photonics

MDPI

Article

Research on Integrated Technology for Simultaneous Detection, Ranging, and Data Transmission Using an Optical DSSS Transceiver

Wenfang Jiao [1], Min Zhang [1,2,*], Rui Weng [1], Guosheng Fan [1], Dixiang Zeng [1], Baiqiu Zhao [1] and Xiaonan Yu [1,2]

[1] School of Optoelectronic Engineering, Changchun University of Science and Technology, Changchun 130022, China; 2023100356@mails.cust.edu.cn (W.J.); 2023100359@mails.cust.edu.cn (R.W.); 2023100355@mails.cust.edu.cn (G.F.); yuxiaonan@cust.edu.cn (X.Y.)

[2] National and Local Engineering Research Center of Space Optoelectronic Technology, Changchun University of Science and Technology, Changchun 130022, China

* Correspondence: zhangmin@cust.edu.cn

Abstract

With the development of space laser networks, miniaturization and lightweight design have become inevitable trends in laser terminal development. In laser links, functions such as spot position measurement, ranging, and data transmission are usually performed by multiple independent units. Integrating these three functions can effectively reduce the size of the opto-mechanical structure and save space within the optical transceiver, thereby supporting the lightweight and compact growth of laser terminals. This paper presents an integrated scheme based on an optical direct-sequence spread-spectrum (DSSS) quadrant detector (QD) and regenerative codes, which enables spot position measurement, ranging, and data transmission through an optical transceiver. The core of this approach involves using a code tracking loop to perform correlation gain calculation, phase comparison, and demodulation of the pseudo-noise code-modulated laser signal, thereby achieving all three functions simultaneously. A desktop experimental system was built to test and verify the scheme's accuracy and precision. The system achieved a ranging accuracy of 14 mm (1σ), a spot position measurement accuracy of 0.83 μm (1σ) at the target center, and a communication sensitivity of −31 dBm at a 10^{-4} bit error rate (BER) with a data rate of 1 Kbps. This study provides a reference for future lightweight optical terminals.

Keywords: free-space optical communication; direct sequence spread spectrum; quadrant detector; laser ranging

Check for updates

Received: 22 November 2025
Revised: 14 December 2025
Accepted: 17 December 2025
Published: 27 January 2026

Copyright: © 2025 by the authors. Licensee MDPI, Basel, Switzerland. This article is an open access article distributed under the terms and conditions of the Creative Commons Attribution (CC BY) license.

1. Introduction

The design of multi-function integration within a single system is conducive to the miniaturization and lightweight development of laser terminals, facilitating the deployment of laser links in more scenarios and improving their operational effectiveness [1–4]. However, traditional laser application systems are predominantly designed for single functionalities: spot position detectors specialize in real-time capture of laser spots for precise targeting and tracking, such as the spot detection algorithm described in reference [5] using a CCD sensor as the spot position detector, and the implementation method for multi-node spot detection described in reference [6] using a QD; laser rangefinders determine distance based on time-of-flight or phase difference measurements [7–10]; while laser communication systems transmit information via intensity or phase modulation [11,12].

Nevertheless, these functionally discrete architectures result in systems with large volume, high power consumption, and elevated costs, posing significant challenges for deployment and application in scenarios with constrained space and resources, such as UAV payloads and satellite platforms.

In recent years, multi-function integration has become an inevitable trend in the development of optoelectronic systems. Among these, integrated ranging and communication have seen relatively extensive development. For instance, in 2011, LISA achieved a communication rate of 24.4 kbps and a ranging accuracy of 42 cm in an inter-satellite link. The ranging-communication integrated scheme proposed for LISA employs heterodyne coherent detection combined with DSSS [13]. In contrast, this study adopts a direct detection approach integrated with DSSS. By eliminating the requirement for a local oscillator laser and a complex heterodyne interference architecture, the proposed scheme achieves a more compact form factor and lower power consumption. Furthermore, it inherently supports scalability for multi-node operational scenarios. [13]; in 2013, the LLCD demonstrated a lunar downlink rate of 622 Mbps, an uplink rate of 19.44 Mbps, and a ranging accuracy of 1 cm. However, the fixed duration of its downlink frame restricts the maximum measurable time delay, resulting in a range ambiguity of approximately 58.5 km. This necessitates reliance on ephemeris data for resolution, which compromises operational flexibility. In contrast, the pseudo-noise (PN) code can inherently circumvent this issue through its long-period characteristics or by directly encoding time information [14]. In 2022, the CubeSat Laser Infrared CrosslinK (CLICK) project planned to achieve a crosslink communication rate of $\geq$20 Mbps between CLICK-B and CLICK-C with a ranging accuracy better than 50 cm. It employs Pulse Position Modulation (PPM), utilizing the communication pulse signals as ranging references. By means of inter-satellite bidirectional laser transmission, the system calculates the distance by measuring the round-trip time difference in the signals. Its ranging-communication system and the spot position detection system are of a discrete architecture. In this study, we integrate these functionalities into a unified transceiver system, thereby further simplifying the hardware design. [15]. Research on integrated spot detection and communication has also made some progress recently. Reference [16] investigated the impact of spreading gain in pseudo-noise code modulation on both communication performance and spot detection accuracy. The study in reference [17] focuses on integrating laser communication and tracking based on a QD for lightweight laser communication ATP (Acquisition, Pointing, and Tracking) systems. The communication functionality employs PPM and Reed-Solomon (RS) encoding to enhance anti-interference capability. Meanwhile, reference [18] proposes a novel Avalanche Photodiode (APD) array to address the complexity of simplifying optomechanical design, where this device can simultaneously support both communication and spot detection functions. Building upon the integration of spot detection and data transmission, this study incorporates ranging functionality, which further simplifies the hardware and improves the space utilization efficiency of the optical transceiver module.

Owing to their broad spectral response, high sensitivity, customizable energy band structure, and fast response speed, QDs can realize functionalities such as spot detection, ranging, data transmission, and angle measurement, making them an ideal choice for integrated laser multi-function systems. This paper focuses on the study of an integrated system for laser spot detection, ranging, and data transmission based on a QD combined with optical DSSS. Utilizing optical DSSS and phase-locking via a code tracking loop, data transmission and ranging functions are achieved, analogous to GPS positioning systems and the ranging subsystem in LISA [19,20]. The relative spot position on the target surface is calculated from the optical power reflected by the correlation peaks in each quadrant of the QD. To eliminate clock offset between both ends for obtaining the ranging result,

the system employs a regenerative pseudo-code ranging method. It demonstrates the implementation of a digital regenerative sequence transceiver in an FPGA: binary pseudo-codes are generated and used to modulate the laser signal at one end; after receiving the modulated signal, the other end performs phase locking, denoises the locked pseudo-codes, and then modulates them back onto a laser transmitter to return to the originating end; finally, phase comparison at the originating end, after compensating for transceiver delays, yields the distance. Furthermore, to enhance the position measurement accuracy of the QD, pseudo-codes with high spreading gain are applied in the laser link, significantly improving the signal-to-noise ratio and consequently the spot position measurement accuracy. This paper describes the system design architecture for spot detection, ranging, and data transmission, and provides experimental validation of the system performance.

2. System Structure

The overall system structure is illustrated in Figure 1. The signal is modulated using DSSS. The original signal is transmitted from the master terminal, while the slave terminal aligns the phase of the local pseudo-noise code with the received signal. The aligned pseudo-noise code is then transmitted back to the master terminal, where it is received by a QD. The master terminal performs phase locking, compares the transmitted and received phases, calculates the relative power in each quadrant, and demodulates the spread spectrum signal. This process simultaneously enables spot detection, ranging, and data transmission.

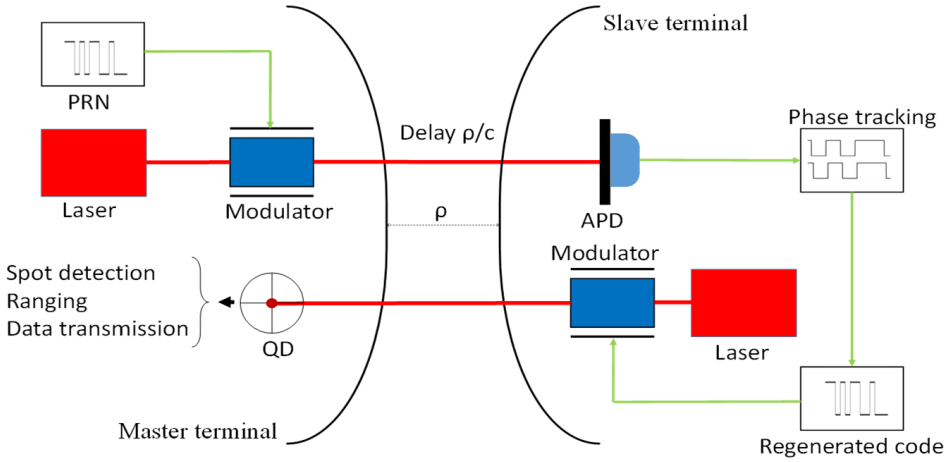


Figure 1. Overall system structure.

2.1. PN Code Generation

The selection of the PN code length is the result of a comprehensive trade-off among various system parameters, primarily involving the balance among spreading gain, data transmission rate, and computational resources. Shorter PN codes offer lower spreading gain and weaker anti-jamming capability, which is detrimental to improving the accuracy of both ranging and spot detection. Although longer PN codes can provide higher spreading gain and enhanced anti-jamming performance, they simultaneously increase the processing time for correlation operations, consume more computational resources, and significantly reduce the achievable data transmission rate. The 1023-bit code length represents an optimal trade-off for the system under study in this work: the corresponding gain is sufficient to ensure reliable spread-spectrum demodulation in the intended operational environment, while maintaining reasonable acquisition time and low synchronization overhead. Moreover, this code length aligns with established standard hardware implementations, thereby enabling feasible deployment on resource-constrained embedded platforms without introducing excessive memory consumption or computational burdens associated with longer

codes. Furthermore, the adoption of Gold codes, which feature low cross-correlation values and sharp auto-correlation peaks, contributes to stable phase locking and also facilitates future scalability in terms of the number of system nodes.

The PN code adopts the same configuration as the GPS standard [21], with a chip rate of 1.023 Mbps. This PN code is generated by modulo-2 addition of two 1023-bit linear sequences, G1 and G2, which are produced by 10-stage shift registers. The generator polynomials for these registers are as follows:

$$G1(x) = 1 + x^3 + x^{10}, \tag{1}$$

$$G2(x) = 1 + x^2 + x^3 + x^6 + x^8 + x^9 + x^{10}. \tag{2}$$

Figure 2 shows the configuration where $r_i{}^1$ (i denotes the register stage number, $i = 1, \ldots, 10$) generates the G1 sequence while $r_i{}^2$ produces the G2 sequence, with registers 2–10 being clock-driven cascaded updates and register 1 updated by feedback value F. The complete process is mathematically represented as:

$$G1 \Rightarrow \begin{cases} F = r_3^1 \oplus r_{10}^1 \\ r_1^1 = F \\ r_i^1 = r_{i-1}^1, i = 2, \cdots, 10 \end{cases} \tag{3}$$

$$G2 \Rightarrow \begin{cases} F = r_2^2 \oplus r_3^2 \oplus r_6^2 \oplus r_8^3 \oplus r_9^2 \oplus r_{10}^2 \\ r_1^2 = F \\ r_i^2 = r_{i-1}^2, i = 2, \cdots, 10 \end{cases} \tag{4}$$

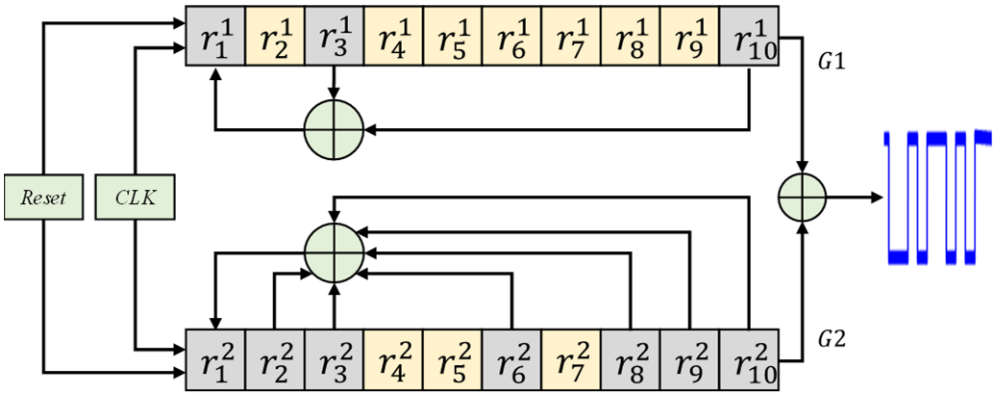


Figure 2. Pseudocode sequence generation principle.

The final spread-spectrum PRN code sequence is generated through the modulo-2 addition of G1 and G2 sequences.

2.2. System Operating Principle

The operational architecture of the master terminal is shown in Figure 3. The master transmits a modulated optical signal that is regenerated by the slave terminal and retransmitted back to the master. After the system acquires the returned optical signal, it performs acquisition and tracking to determine the relative optical power distribution across four quadrants, which is used to calculate the spot position relative to the detector, while simultaneously obtaining the phase information of the returned signal. By comparing the transmitted pseudocode phase with the locally tracked pseudocode phase, the phase difference is derived to calculate the time-of-flight (ToF) and subsequently obtain distance information.

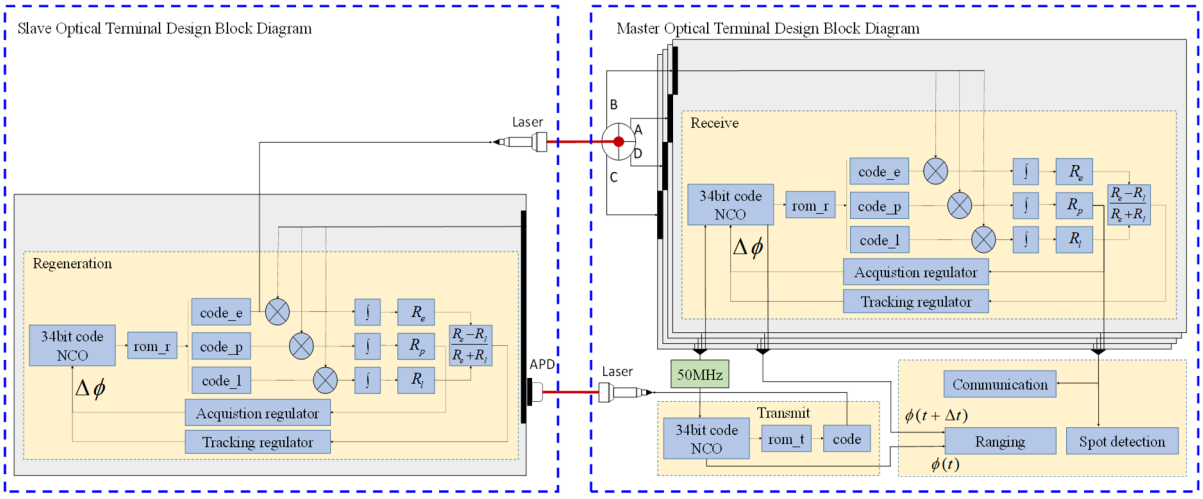


Figure 3. Signal processing structure. (A, B, C, D represent the signals from the 1st, 2nd, 3rd, and 4th quadrants of the QD, respectively.)

For pseudocode tracking, correlation-based feedback control is employed. The system generates delayed versions of the locally tracked code to produce an early code, a prompt code, and a late code, which are then correlated with the received signal to obtain the early correlation value R_E, the prompt correlation value R_P, and the late correlation value R_L. (The symbols used in the formulas are further summarized in Appendix A.) The correlation algorithm is as follows:

$$R_{E,P,L}(\tau) = \frac{1}{T}\int_0^T s_{rs}(t)s_{E,P,L}(t)dt, \tag{5}$$

where T represents the integration time. In the above formula, the prompt code correlation result R_P is used for the tracking threshold decision. By comparing R_P with the acquisition threshold, the local code phase is adjusted in 1/2-chip steps. With this 1/2-chip precision, the ranging code and local code can achieve precise alignment. The system then enters the tracking state, performing normalized phase discrimination on the preamble and prompt code correlation results (R_E and R_L) to achieve exact chip alignment. The phase discrimination is based on the following formula:

$$codeError = \frac{R_E - R_L}{R_E + R_L}. \tag{6}$$

This formula is applicable to the phase tracking stage after successful phase acquisition. Since the scanning step size during the phase acquisition phase is 1/2 chip, the chip alignment accuracy is within $\pm 1/2$ chip. Within this range, the formula's output maintains a linear relationship with the chip phase deviation. When the phase alignment deviation leads by 1/2 chip, $R_E = 0$, $R_L = 1$, and codeError = -1. When the alignment deviation lags by 1/2 chip, $R_E = 1$, $R_L = 0$, and codeError = 1. When the phase alignment deviation is zero, $R_E = R_L$ and codeError = 0.

This normalized code phase error result is connected to a low-pass filter to produce an NCO frequency-control word, which adjusts the local code phase to synchronize with the input code sequence, and this algorithm is as follows:

$$\delta\phi_{rs}(k) = \delta\phi_{rs}(k-1) + \frac{t_i}{\tau_1} * codeError + \frac{\tau_2}{\tau_1} * [codeError - oldcodeError], \tag{7}$$

$$\phi_{rs}(k+1) = \phi_{rs}(k) + \delta\phi_{rs}. \tag{8}$$

In the controller algorithm, *codeError* is the current output value of the phase detector, and *oldcodeError* is the output value of the phase detector from the previous integration period, t_i is the integration time, $\tau_1 = k/\omega_0^2$ and $\tau_2 = 2\zeta/\omega_0$ are the loop parameters that determines the natural frequency ω_0 and damping ratio ζ of the system, and k is the filter coefficient, $\phi_{rs}(k)$ is the code frequency. $\delta\phi_{rs}$ adjusts the local code phase by modifying the NCO accumulator to align the input signal with the reference signal.

Figure 4 illustrates the variation in the absolute prompt correlation value during phase acquisition and tracking. When the prompt correlation value is below the threshold, the code tracking loop scans the received signal with half-chip phase steps. Once the correlation value exceeds the threshold, tracking is performed based on the normalized phase error, where pseudocode phase control maintains the correlation value at its maximum level. During stable tracking, the sign bit of the correlation value is employed for demodulation of data transmission signals to achieve data transmission.

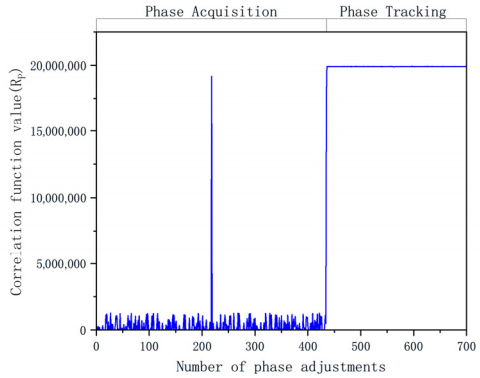


Figure 4. Variation in correlation values during phase acquisition and tracking.

After code phase alignment, the generated stable correlation peak reflects the optical power covering the corresponding QD quadrant, from which the spot position can be determined based on the optical power distribution across quadrants.

$$x_r = \frac{R_A + R_D - R_B - R_C}{R_A + R_D + R_B + R_C} \tag{9}$$

$$y_r = \frac{R_A + R_B - R_C - R_D}{R_A + R_B + R_C + R_D} \tag{10}$$

(x_r, y_r) denotes the relative position coordinates, R_A, R_D, R_B, and R_C represent the instantaneous correlation peaks for each channel of the QD. According to Reference [20], for the off-axis results, transformations from relative to absolute coordinates were established. Taking the x-axis as an example, the absolute coordinate is as follows:

$$x_o = \frac{\omega}{\sqrt{2}} erf^{-1}(x_r), \tag{11}$$

$$y_o = \frac{\omega}{\sqrt{2}} erf^{-1}(y_r), \tag{12}$$

where (x_o, y_o) represents the absolute position coordinates, ω is the spot radius, with an experimental value of 1.05 mm.

After code chip synchronization, the phase comparison between transmitted and received signals is performed for ranging measurement.

The ranging system employs a regenerative code ranging method, where the master terminal transmits ranging pseudocode that is received and retransmitted by the slave terminal. The master terminal then compares the transmission and reception phases to

determine the transit time, while compensating for the transmission/reception time delays at both terminals to eliminate clock offset between master and slave units, thereby achieving accurate channel distance measurement.

First, after both systems start operating, the master optical terminal transmits the ranging code, which undergoes the transmission time T_1 before the laser enters the spatial link and propagates with the corresponding propagation time T_2 to reach the receiving target surface of the slave optical terminal. After experiencing the reception time T_3 at the slave terminal, the signal enters the phase-locked turnaround process with a turnaround time T_4. The regenerated pseudocode signal is then delivered to the laser modulator, and after the transmission time T_5 at the slave terminal, the optical signal is transmitted back through the spatial link. After another propagation time T_2, the optical signal arrives at the target surface of the master optical terminal. Following the reception time T_6 at the master terminal, the returned ranging signal suitable for phase comparison is obtained. By comparing the phase of the returned signal with that of the transmitted signal, the total optical signal transit time t_1 is determined. For the measurement of (T_1, T_3, T_4, T_5, T_6), this study determines these components by measuring the total delay time t_1 at a known distance. By subtracting the known spatial propagation delay $2T_2$ from t_1, the combined value $T_1 + T_3 + T_4 + T_5 + T_6$ is obtained. This value is recorded in the calibration procedure. In subsequent measurements, $T_1 + T_3 + T_4 + T_5 + T_6$ is directly subtracted from the measured t_1, thereby allowing the immediate determination of $2T_2$.

The speed of light in vacuum is c. The expression for distance ρ is as follows:

$$\rho = \frac{1}{2} \cdot (t_1 - T_1 - T_3 - T_4 - T_5 - T_6) \cdot c. \tag{13}$$

Regarding data transmission, the received data bit d can be recovered based on the sign of the correlation value R_P. The decision rule is as follows:

$$d \Rightarrow \begin{cases} 1, R_P \geq 0 \\ 0, R_P < 0 \end{cases}. \tag{14}$$

3. Accuracy Analysis

According to Reference [22], the relationship between position detection precision and SNR is given as follows:

$$\sigma_{x_0} \approx \frac{\sqrt{\pi}\omega}{2\sqrt{2}} \cdot \frac{1}{\sqrt{SNR}} \cdot \sqrt{1 + erf^2\left(\frac{\sqrt{2}x_0}{\omega}\right)}. \tag{15}$$

In spread spectrum communication systems, the SNR of the output signal shows improvement compared to that of the received signal at the receiver after despreading. The ratio of the output SNR to the input SNR in the receiving system is defined as the spreading gain, whose mathematical expression equals the ratio of the post-spreading bandwidth to the pre-spreading bandwidth.

$$G_p = \frac{SNR_{out}}{SNR_{in}}, \tag{16}$$

where SNR_{out} denotes the SNR of the despread output signal, and SNR_{in} represents the SNR of the input signal before despreading. According to Equation (15), the total SNR after despreading relates to the SNR of the photoelectric signal received by the detector as follows:

As evident from Figure 5, under identical SNR conditions, the position detection precision of the QD improves with increasing spreading gain.

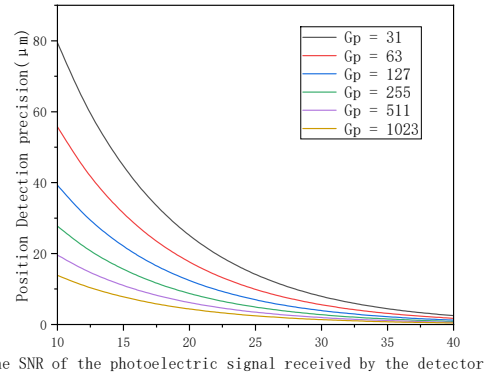


Figure 5. The influence of different SNRs and spreading gains on the position detection precision of the detector.

The primary contributors to ranging error are processor clock inaccuracies and PLL errors. Reference [23] provides an error model for PLL-induced deviations, expressed as

$$\sigma_{DLL} = c \cdot T_c \sqrt{\frac{B_n}{C/N_0}}, \tag{17}$$

where T_c represents the code chip period, B_n denotes the loop bandwidth configured for the PLL, and B_n is calculated as follows:

$$B_n = \frac{1}{8}\omega_0\left(4\zeta + \frac{1}{\zeta}\right), \tag{18}$$

where C/N_0 indicates the carrier-to-noise ratio. Taking the laser link's C/N_0 ratio of 60–95 dB-Hz as an example [13]. For direct power detection, the SNR_{in} can be directly characterized by its C/N_0, approximately as $SNR_{in} \approx C/N_0$. Therefore, the ranging detection accuracy can also be expressed as:

As illustrated in Figure 6, under constant SNR_{in} conditions, the measurement precision improves with reduced loop bandwidth. However, in practical implementations, excessively narrow bandwidth settings would compromise the PLL synchronization capability. Therefore, the system adopts a 20 Hz loop bandwidth as the operational optimum, balancing tracking stability and noise rejection.

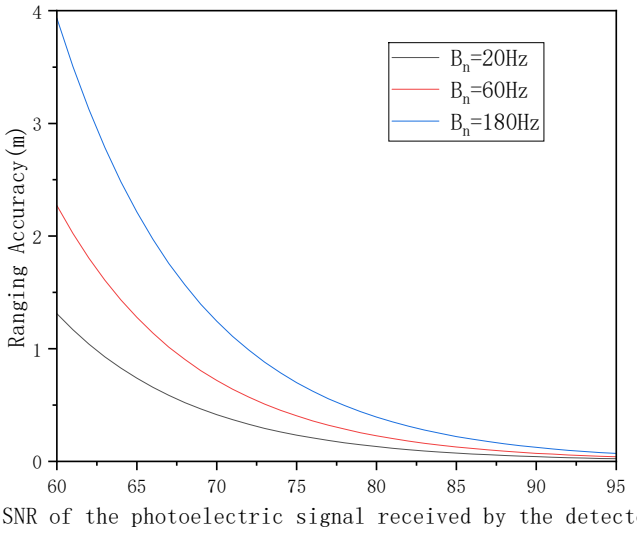


Figure 6. Influence of Different SNRs and loop bandwidths on ranging accuracy.

One source of ranging error stems from inaccuracies in the clock signal used for the PN code tracking loop, including both receiver-generated clock signals and clock source-induced errors.

$$\Delta T = T_0 - T = \frac{N}{f_n} - \frac{N}{f} = \frac{N(f - f_n)}{f_n f} \approx T_0 y, \tag{19}$$

where is the FPGA frequency count, f_n is the reference clock frequency, f is the actual clock frequency, and $y = (f - f_n)/f_n$ is the frequency error. This allows the determination of the ranging error impact from different clock source types. The ranging error per 100 km caused by clock errors is shown in the following figure:

In Figure 7, XO represents a standard crystal oscillator. The temperature-compensated crystal oscillator (TCXO) employs temperature-compensated crystals, while the OCXO is an oven-controlled crystal oscillator. Furthermore, atomic clocks demonstrate significantly higher precision than crystal oscillators, as exemplified by: rubidium atomic clocks with frequency error ranges of 10^{-4}–10^{-2} ppm; cesium atomic clocks achieving frequency accuracy of 10^{-6}–10^{-5} ppm; and hydrogen maser clocks attaining 10^{-7}–10^{-8} ppm frequency precision. For our experimental validation of ranging performance, we utilized a TCXO.

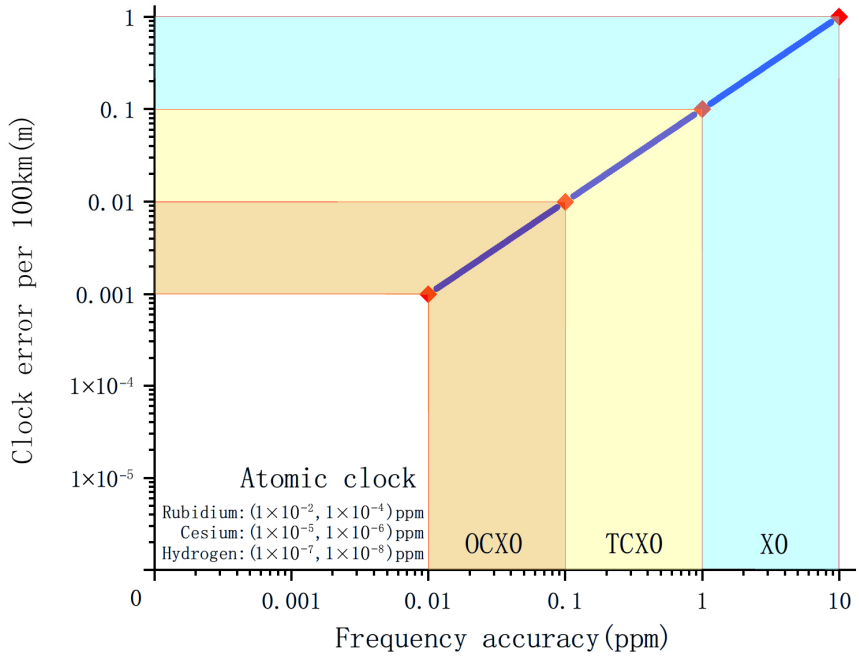


Figure 7. Impact of Clock Errors on Ranging Accuracy.

4. Experimental Results and Analysis

Figure 8 illustrates the experimental architecture employed in this study. The setup utilizes a benchtop platform, with a QD serving as the master terminal detector and an avalanche photodiode (APD) as the slave terminal detector. The master terminal transmits a PN code to the slave terminal. Upon reception, the slave terminal performs phase alignment and retransmits the signal back to the master terminal. The returned signal is captured by the QD at the master terminal and subsequently relayed to a processing unit. This processor performs the necessary computations to enable the concurrent operation of spot position measurement, ranging, and data transmission.

Based on the preceding system analysis and design, the aforementioned benchtop experimental system, as shown in Figure 9, was implemented to verify.

(1) Spot detection accuracy in spatial optical links;
(2) Laser ranging accuracy;
(3) Data transmission.

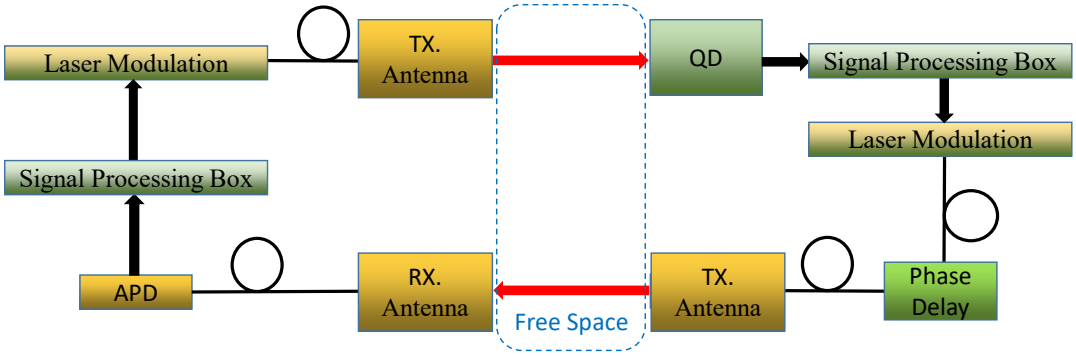


Figure 8. Schematic Diagram of Experimental Setup. (The circles represent optical fibers).

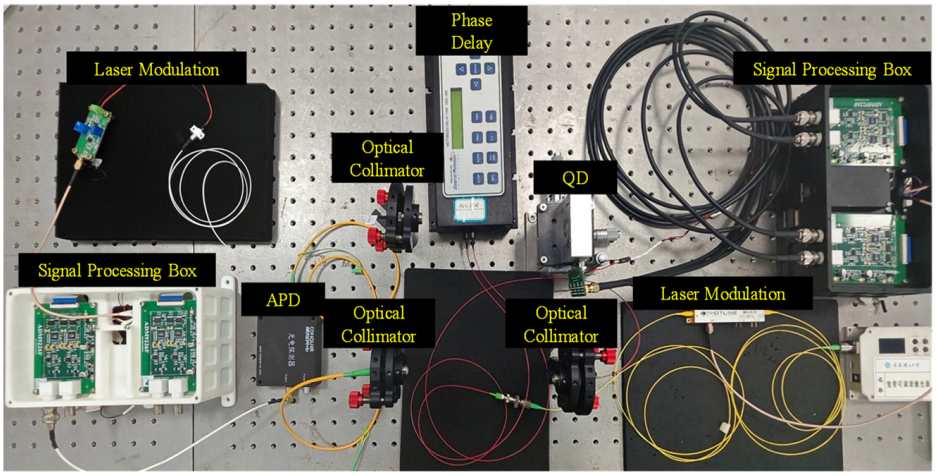


Figure 9. Experimental Setup Diagram.

The spot detection experimental results are as follows:

In the experiment, the diameter of the photosensitive area of the QD is 4 mm. When the light spot is at the center of the QD's photosensitive area, the host computer display and the QD target photograph are shown in Figure 10.

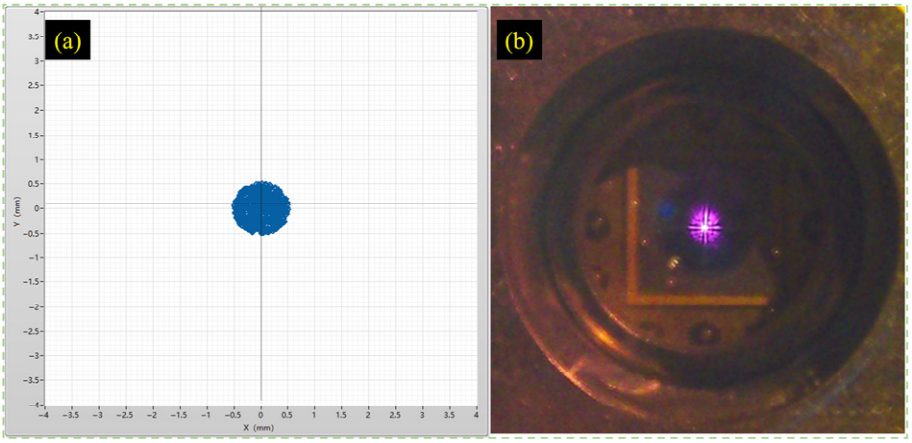


Figure 10. (**a**) Detection result host computer image (**b**) Image of the quadrant detector.

In Figure 11, the "homologous signal" is both generated and received by the master terminal itself using its laser source and QD. In contrast, the "regenerated signal" is transmitted by the master terminal to the slave terminal, where it is modulated and sent back to be received by the master terminal's QD.

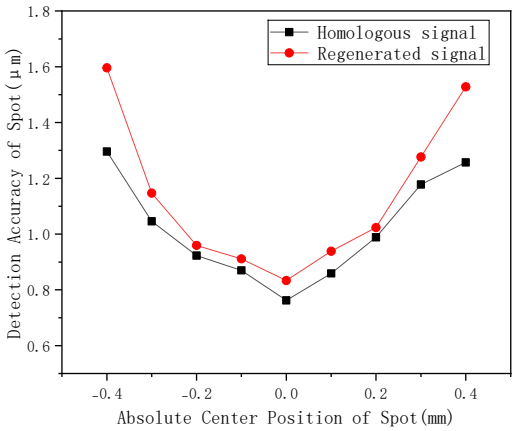


Figure 11. Position Detection Accuracy under Different Conditions and Locations.

The experiment utilized a translation stage to vary the relative position between the light spot and QD, as well as the signal source, thereby validating the accuracy of spot position measurement and functional integration. By displacing the spot position along the *x*-axis, the position detection accuracy at different locations was recorded. As shown in Figure 11, the experimental results demonstrate that the detection accuracy at the QD target center surpasses that of other positions. Data indicate that the average positional detection error measured at each point under the regenerated signal condition is 0.115 μm higher than that under the homologous signal condition. Moreover, the difference in positional detection accuracy is smaller near the center compared to that near the edges.

To investigate the universality of the spot detection function under varying incident angles, a QD was mounted on an optical base capable of azimuthal rotation. The detection accuracy for the spot at three positions on the *x*-axis—0 mm, +0.3 mm, and +0.6 mm—was compared across different rotation angles. The results are shown in Figure 12.

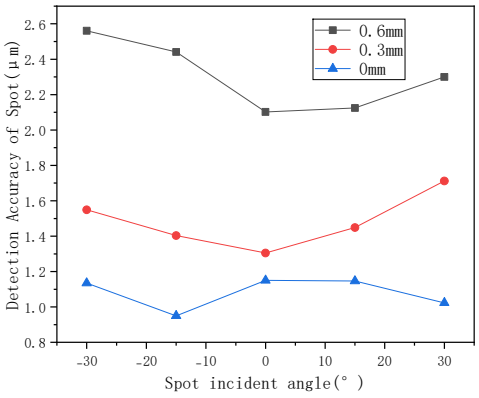


Figure 12. The variation in spot position detection accuracy at different points on the QD under varying incident angles.

The results indicate that positions closer to the edge are more significantly affected by angular variations. Under incident angle changes of ±30°, the maximum fluctuation in spot position detection accuracy is approximately 0.46 μm at the +0.6 mm location, about 0.41 μm at the +0.3 mm location, and around 0.20 μm at the 0 mm location.

The ranging experimental results are as follows:

In Figure 13b "Equivalent delay distance" refers to the equivalent distance achieved through fiber-optic delay lines, while "Range" denotes the distance measured under the corresponding delay condition.

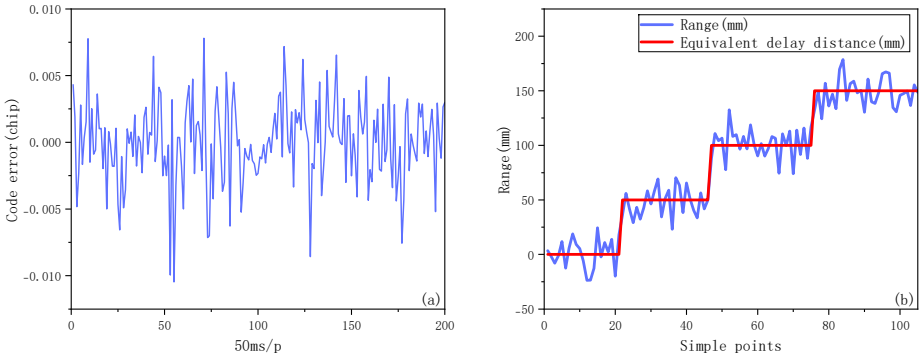


Figure 13. (**a**) Signal phase tracking error. (**b**) Ranging results.

The ranging measurement accuracy was verified by installing a fiber-optic programmable delay line (General Photonics MDL-002) at the master terminal to adjust the link delay. This phase calibration standard device features a 500 ps delay range with 10 fs-level precision, fully satisfying millimeter-scale distance calibration requirements [24]. During experiments, phase locking was used to ensure frequency and phase alignment between the dual-terminal laser links. Figure 13a shows the pseudocode chip alignment accuracy during ranging, with a phase standard deviation of 0.003 chips (1σ). After processing through the loop filter, the ranging result can be derived based on the NCO phase. In practice, owing to the low-pass filtering effect and the additional filtering applied to the ranging results, the random ranging error becomes smaller than the range error corresponding to the phase tracking error. Figure 13b shows the variation in the ranging readings as the fiber delay line is stepped in increments of 50 mm from 0 to 150 mm.

Experimental results demonstrate the system's response to distance variations, with a measurement standard deviation of 14 mm (1σ). Additionally, to verify whether the ranging function is capable of measuring over longer distances, we employed a software-based simulation approach in which the processor applied a fixed time delay to the ranging signal and successively increased the delay duration. The results are shown in the Figure 14:

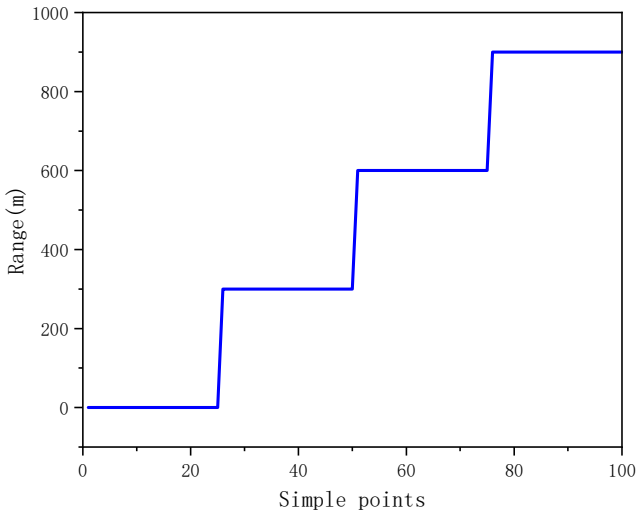


Figure 14. Simulated Long-Distance Ranging Results.

In this experiment, the chip rate is primarily constrained by the hardware bandwidth of the QD, which is 8 MHz. To preserve as sharp a waveform edge as possible and ensure phase-locking accuracy, a chip frequency of 1.023 MHz was selected. Meanwhile, to maintain high spreading gain, a spreading sequence with a length of 1023 chips was employed. If a higher data transmission rate is required, a QD device with a larger bandwidth can be customized to support an increased chip rate. Alternatively, in scenarios

where detection accuracy and ranging precision are less critical, a spreading sequence with a shorter code length can be employed to enhance the data transmission rate. For instance, a PN code with a length of 511 chips can increase the data transmission rate to 2 kbps, while a PN code with a length of 255 chips can further elevate the data transmission rate to 4 kbps.

The system achieved -31 dBm sensitivity at a BER of 10^{-4} under 1 Kbps data transmission.

The demodulated data waveform is shown below:

The data transmission function was tested by modulating a 127-bit PN code onto a spread-spectrum signal. The receiver demodulated the signal, performed bit error counting, and output the demodulated signal at the TTL level for oscilloscope observation. As shown in Figure 15a, a complete demodulated PN code cycle demonstrates that the data transmission function is capable of delivering intact signals. The displayed waveform corresponds to a bit error rate of 9.3×10^{-6}. The bit error rate was derived by collecting and comparing a total of 326,467 bits, with 3 erroneous bits detected, from which the result was calculated.

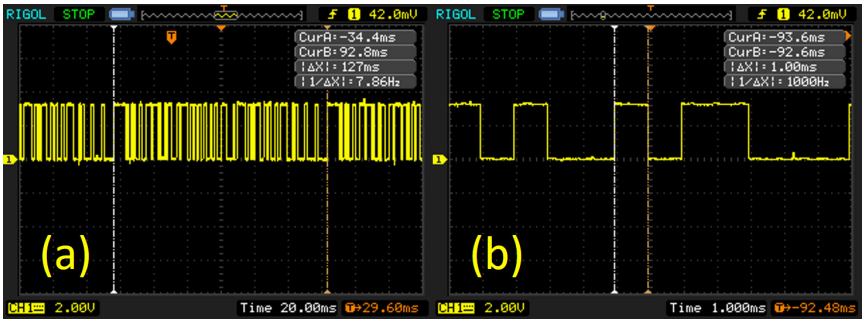


Figure 15. The binary data transmission data output via TTL levels. (**a**) Full-period PN code signal (**b**) Single chip.

5. Discussion

To ensure spot detection accuracy and ranging performance, this study employs a long PN code sequence of 1023 bits to achieve high spreading gain. However, this choice comes at the expense of data transmission rate, resulting in a transmission rate of only 1 Kbps, which is lower than that of comparable integrated ranging and communication systems such as LISA (24.4 kbps) and LLCD (up to 622 Mbps). Furthermore, without upgrading the detector's bandwidth, the primary approach to increase the data transmission rate in this system is to shorten the PN code length. This reduction would directly decrease the spreading gain, leading to a degradation in both spot detection and ranging accuracy, thereby creating a fundamental trade-off between "data transmission rate" and "ranging/detection precision." Therefore, future work will continue to explore new modulation and detection schemes. Additionally, as the current experiments were conducted solely on an optical bench, it remains difficult to validate the system's performance over long-distance atmospheric channels. For evaluating its performance under real-world, extended-range conditions, future work will involve integrating the setup into an actual optical transceiver module for field testing.

It should be noted that the spread-spectrum transmission architecture of this system, which is similar to the CDMA-based codomain detection framework reported in Ref. [22], theoretically supports multi-node signal identification and parallel spot detection due to the excellent cross-correlation orthogonality of the adopted Gold codes. However, the current experimental validation of the system is limited to single-node signal interaction scenarios, and no targeted tests have been conducted for multi-channel signal superposition and multi-node collaborative operation. Specifically, the system has not yet been verified in scenarios

involving simultaneous access of multiple slave nodes, including key performance metrics such as mutual interference between multi-node signals, the upper limit of identifiable node quantity, and the stability of spot position measurement for each node under multi-signal coupling conditions.

In subsequent research, we will prioritize the construction of a multi-node collaborative test platform to carry out systematic verification of multi-node-related functions. First, we will conduct experiments on multi-node simultaneous spot detection, focusing on exploring the influence of code sequence allocation and signal power differences on the detection accuracy of each node's spot position, and verifying whether the master terminal can stably distinguish and locate the spots of multiple nodes at the QD. On this basis, we will further expand the research scope to multi-node collaborative ranging: for multi-node ranging, we will focus on solving technical bottlenecks such as phase synchronization between multiple slave terminals, ranging priority scheduling, and elimination of ranging error interference caused by signal superposition.

Looking forward, after completing the verification and optimization of multi-node functions, the master detection system is expected to evolve into a highly integrated optical transceiver platform that integrates multi-node spot detection, high-precision ranging, and data transmission. This upgraded system will be able to meet the application demands of distributed scenarios such as satellite constellations and UAV swarms, and further promote the functional integration and lightweight development of laser terminals.

6. Conclusions

This paper thoroughly explores the integrated fusion design of an optical transceiver for multifunctional applications from three perspectives: mechanism, error analysis, and experimental evaluation. Desktop experiments were performed to verify the feasibility and performance of each function under multifunctional multiplexing conditions. The ability of spreading gain to suppress position detection error was analyzed, and the effects of different loop bandwidths on ranging accuracy were examined. The influence of the processor's clock source on the system's ranging error was also assessed. The ranging system used a dual one-way signal regeneration method to eliminate clock bias, ensuring that the laser signal incident on the QD target surface was a regenerated laser signal. As a result, the laser signal received by the QD target surface contained phase noise introduced by the slave tracking loop. Therefore, experiments were conducted to evaluate the performance of spot detection and data transmission functions under regenerated signal conditions compared to non-regenerated conditions. The results show that the regenerated signal has minimal impact on data transmission sensitivity. The center spot position measurement error under regenerated signal conditions was 0.83 μm (1σ), slightly higher than the 0.76 μm (1σ) under non-regenerated conditions but still within acceptable limits. In practical systems, when the laser link is successfully established, the spot is typically located at the center of the QD target surface. Ranging was thus performed with the spot at this position. The results indicate that the system can accurately detect distance changes, achieving a ranging accuracy of 14 mm(1σ). For the data transmission system, the adoption of a longer PN code sequence with substantial spreading gain in this experiment was necessary to ensure both spot detection accuracy and ranging precision; however, this implementation, combined with the inherent bandwidth limitations of the hardware components, resulted in a constrained data transmission rate of 1 Kbps. Although the current data transmission rate is relatively low, we plan to increase the chip rate in future studies by employing a custom QD with higher bandwidth. Meanwhile, for scenarios where ranging accuracy and detection precision are less critical, shorter PN codes can be adopted, and more efficient shorter codes will be explored to enhance the data transmission

rate. Furthermore, the system is designed for future expansion to multiple optical nodes. In this system, the PN code employs Gold codes, which exhibit excellent inter-code isolation characteristics, making them highly suitable for code-division multiple access (CDMA) systems that require strict user distinction. Therefore, the detection system at the master terminal possesses inherent potential to support multiple optical nodes.

In conclusion, this study provides a valuable reference for future integration of multiple functions into an optical transceiver and the development of lightweight optical terminals.

Author Contributions: W.J.: conceptualization, methodology, software, validation, formal analysis, investigation, data curation, writing—original draft preparation, visualization. M.Z.: writing—review and editing, supervision, project administration, funding acquisition. R.W.: investigation, resources. G.F.: investigation. D.Z.: investigation. B.Z.: investigation. X.Y.: conceptualization, methodology, resources, writing—review and editing, supervision, project administration, funding acquisition. All authors have read and agreed to the published version of the manuscript.

Funding: This research was funded by National Natural Science Foundation of China Youth Fund (62401085) and National Key R&D Program of China (2022YFB3902501).

Institutional Review Board Statement: Not applicable.

Informed Consent Statement: Not applicable.

Data Availability Statement: The original contributions presented in this study are included in the article. Further inquiries can be directed to the corresponding author.

Conflicts of Interest: The authors declare no conflicts of interest.

Appendix A

Table A1. Symbols involved in Equations.

Symbols	Specification	Symbols	Specification
R_E	Early correlation value	c	Speed of light
R_P	Prompt correlation value	d	Data bit
R_L	Late correlation value	σ_{x_0}	Position detection precision
s_{rs}	Received signal	SNR	Signal-to-noise ratio
s_E	Early local code, and the late local code	G_p	Spreading gain
s_P	Prompt local code,	σ_{DLL}	Ranging error due to phase-locked loop
s_L	Late local code	T_c	Chip period
$codeError$	Normalized phase error	B_n	Loop bandwidth
$oldcodeError$	Normalized phase error from the previous integration period	C/N_0	Carrier-to-noise ratio
τ_1, τ_2	Loop parameter	ω_0	Natural frequency
t_i	Integration time	ζ	Damping ratio
$\delta\phi_{rs}$	Phase adjustment	ΔT	Time error
ϕ_{rs}	Pseudocode frequency	T_0	Ideal clock count time
(x_r, y_r)	Relative position coordinates	T	Actual clock count time
(x_o, y_o)	Absolute position coordinates	f_n	Ideal clock frequency
ω	Spot radius	f	Actual clock frequency
ρ	Distance	y	Frequency error

References

1. Palmer, C. NASA Satellite Sets Blistering Optical Communication Speed Record. *Engineering* **2024**, *34*, 9–11. [CrossRef]
2. Watkins, M.M.; Flechtner, F.; Morton, P.; Webb, F. Current Status of the GRACE Follow-On Mission. In *AGU Fall Meeting Abstracts, Proceedings of the Agu Fall Meeting, San Francisco, CA, USA, 12–16 December 2016*; AGU: Washington, DC, USA, 2016.
3. Amaro-Seoane, P.; Audley, H.; Babak, S.; Baker, J.; Barausse, E.; Bender, P.; Berti, E.; Binetruy, P.; Born, M.; Zweifel, P.; et al. Laser Interferometer Space Antenna. *arXiv* **2017**, arXiv:1702.00786. [CrossRef]

4. Gong, Y.; Luo, J.; Wang, B. Concepts and status of Chinese space gravitational wave detection projects. *Nat. Astron.* **2021**, *5*, 881–889. [CrossRef]
5. Liu, X.; Ba, D.; Jiao, D.; Shao, X.; Mu, X.; Wang, Y. Influences of Analog-to-Digital Conversion Accuracy and Response Uniformity of CCD on Small-Scale Laser Focal Spot Measurements. *Laser Part. Beams* **2021**, *2021*, e20. [CrossRef]
6. Yu, X.; Chen, S.; Xu, L.; Weng, R.; Zhao, B.; Zhang, Z.; Lin, P.; Guo, X.; Wang, T.; Song, Y.; et al. A CDMA Method for Multibeacon Codomain Detection by a Quadrant Detector in Free-Space Optical Networking. *J. Light. Technol.* **2025**, *43*, 61–70. [CrossRef]
7. Gao, W.; Zhou, W.; Zhou, S.; Chen, G.; Huang, Y.; Qu, W.; Hu, X. A method for estimating the rotation errors of BDS broadcast ephemeris using global satellite laser ranging data. *Meas. Sci. Technol.* **2024**, *11*, 35. [CrossRef]
8. Wang, Z.; Yang, S.; Jia, F.; Wu, K.; Liao, F.; Duan, H.; Yeh, H.-C. Alternative Approach to Tilt-to-Length Coupling Estimation for Laser Ranging Interferometers in Future Gravity Missions. *Remote Sens.* **2024**, *16*, 862. [CrossRef]
9. Yuan, Y.; Li, X.; Zheng, H.; Gao, C.; Yao, X. Incorporating Satellite Laser Ranging observations into BDS analysis: From the perspectives of orbit validation, precise orbit determination, and geodetic parameters estimation. *J. Geod.* **2025**, *99*, 13. [CrossRef]
10. Wang, J.; Zhu, W.; Gong, W. An efficient real-time signal processing method for satellite laser ranging. *PLoS ONE* **2024**, *19*, e0315375. [CrossRef] [PubMed]
11. Xing, L.; Li, Z.; Huang, Y.; Zhang, Z. Efficient coding schemes for blue–green laser cross-medium communication based on polar codes. *Opt. Eng.* **2025**, *64*, 058106. [CrossRef]
12. Chen, T.; Liu, Z.; Yang, Q.; Meng, J.; Wang, T.; He, J.J.; Li, Q.; Li, M. 4*10 Gbps WDM communication system based on a tunable V-cavity semiconductor laser. *Opt. Express* **2023**, *31*, 28174–28184. [CrossRef] [PubMed]
13. Esteban, J.J.; García, A.F.; Barke, S.; Peinado, A.M.; Cervantes, F.G.; Bykov, I.; Heinzel, G.; Danzmann, K. Experimental demonstration of weak-light laser ranging and data communication for LISA. *Opt. Express* **2011**, *19*, 15937–15946. [CrossRef] [PubMed]
14. Stevens, M.L.; Parenti, R.R.; Willis, M.M.; Greco, J.A.; Khatri, F.I.; Robinson, B.S.; Boroson, D.M. The lunar laser communication demonstration time-of-flight measurement system: Overview, on-orbit performance, and ranging analysis. In *Free-Space Laser Communication and Atmospheric Propagation XXVIII, Proceedings of the SPIE LASE 2016, San Francisco, CA, USA, 13–18 February 2016*; SPIE: Bellingham, WA, USA, 2016; Volume 9739.
15. Tomio, H.; Kammerer, W.; Grenfell, P.; Cierny, O.; Garcia, M.; Lindsay, C.; Belsten, N.; Serra, P.; Cahoy, K.; Clark, M.; et al. Transmitter and fine pointing system development and testing for the CubeSat Laser Infrared Crosslink (CLICK) B/C mission. In Proceedings of the 2023 SPIE, San Francisco, CA, USA, 28 January–2 February 2023; Volume 12777.
16. Chen, S.; Yu, X.; Ye, J.; Lin, P.; Zhang, Z.; Wang, T.; Xu, L. High-Precision Position Detection and Communication Fusion Technology Using Beacon Spread-Spectrum Modulation with Four-Quadrant Detector. *Appl. Sci.* **2024**, *14*, 3362. [CrossRef]
17. Zhang, Y.; Wang, Y.; Deng, Y.; Du, A.; Liu, J. Design of a Free Space Optical Communication System for an Unmanned Aerial Vehicle Command and Control Link. *Photonics* **2021**, *8*, 163. [CrossRef]
18. Rabinovich, J.; Ferraro, M.S.; Page, T.A.; Thomas, L.M.; Rabinovich, W.S.; Mahon, R.; Menas, A.J. Effects of combinatorial sensing on tracking algorithms for FSO systems. In *Free-Space Laser Communications XXXII*; SPIE: Bellingham, WA, USA, 2020; Volume 55.
19. Menn, M. Autonomous navigation for GPS via crosslink ranging. In Proceedings of the PLANS '86-Position Location and Navigation Symposium, Las Vegas, NV, USA, 4–7 November 1986.
20. Yamamoto, K.; Bykov, I.; Reinhardt, J.N.; Bode, C.; Grafe, P.; Staab, M.; Messied, N.; Clark, M.; Heinzel, G. Experimental end-to-end demonstration of intersatellite absolute ranging for LISA. *Phys. Rev. Appl.* **2024**, *22*, 054020. [CrossRef]
21. Glennon, E. Cross Correlation Mitigation for C/A Code GPS Receivers. Doctoral Dissertation, The University of New South Wales, Sydney, Australia, 2009. [CrossRef]
22. Weng, R.; Zhang, M.; Fan, G.; Jiao, W.; Lin, P.; Zhang, Z.; Zeng, D.; Yu, X. Research on a CDMA-Based Integrated Single-Terminal Detection System for Laser Communication Networking with Micrometer-Level Disturbance Error. *Opt. Commun.* **2025**, *586*, 131928. [CrossRef]
23. Yu, X.; Tong, S.; Zhao, X.; Jiang, J.; Chen, X. Two-way laser regeneration pseudocode rangefinder of intersatellite optical crosslink. *Opt. Eng.* **2020**, *59*, 036101. [CrossRef]
24. Photonics, G. *MDL-002 Miniature Motorized Variable Optical Delay Line Operation Manual*; Version:1.3; General Photonics Corporation: Chino, CA, USA, 2015.

Disclaimer/Publisher's Note: The statements, opinions and data contained in all publications are solely those of the individual author(s) and contributor(s) and not of MDPI and/or the editor(s). MDPI and/or the editor(s) disclaim responsibility for any injury to people or property resulting from any ideas, methods, instructions or products referred to in the content.